HHS Public Access

Author manuscript

Clin Cancer Res. Author manuscript; available in PMC 2020 January 15.

Published in final edited form as:

Clin Cancer Res. 2019 January 15; 25(2): 552–561. doi:10.1158/1078-0432.CCR-18-1233.

Identifying Recurrent Malignant Glioma after Treatment Using Amide Proton Transfer-Weighted MR Imaging: A Validation Study with Image-Guided Stereotactic Biopsy

Shanshan Jiang[1], **Charles G. Eberhart**[2], **Michael Lim**[3], **Hye-Young Heo**[1], **Yi Zhang**[1], **Lindsay Blair**[4], **Zhibo Wen**[7], **Matthias Holdhoff**[5], **Doris Lin**[1], **Peng Huang**[5], **Huamin Qin**[2], **Alfredo Quinones-Hinojosa**[3], **Jon D. Weingart**[3], **Peter B. Barker**[1], **Martin G. Pomper**[1], **John Laterra**[4,6,8], **Peter C.M. van Zijl**[1,8], **Jaishri O. Blakeley**[4], and **Jinyuan Zhou**[1,8]

[1]Departments of Radiology, Johns Hopkins University, Baltimore, Maryland, USA

[2]Departments of Pathology, Johns Hopkins University, Baltimore, Maryland, USA

[3]Departments of Neurosurgery,Johns Hopkins University, Baltimore, Maryland, USA

[4]Departments of Neurology,Johns Hopkins University, Baltimore, Maryland, USA

[5]Departments of Oncology, Johns Hopkins University, Baltimore, Maryland, USA

[6]Departments of Neuroscience, Johns Hopkins University, Baltimore, Maryland, USA

[7]Department of Radiology, Zhujiang Hospital, Southern Medical University, Guangzhou, Guangdong, China

[8]F.M. Kirby Research Center for Functional Brain Imaging, Kennedy Krieger Institute, Baltimore, Maryland, USA

Abstract

Purpose: To quantify the accuracy of amide proton transfer-weighted (APTw) MRI for identifying active glioma post-treatment via radiographically guided stereotactic tissue validation.

Experimental Design: Twenty-one patients referred for surgery for MRI features concerning for tumor progression versus treatment effect underwent pre-operative APTw imaging. Stereotactic biopsies were taken from regions of interest with varying APTw signal intensities. The relationship between final clinical pathology as well as the histopathology of each of the 64 specimens was analyzed relative to APTw results. Analysis of confirmed recurrent tumor or treatment effect tissue was used to perform receiver-operating-characteristic (ROC) analysis.

Corresponding Authors: Jinyuan Zhou, Ph.D., Department of Radiology, Johns Hopkins University, 600 N. Wolfe Street, Park 336, Baltimore, MD 21287, USA. Phone: (410) 955-7491, Fax: (410) 614-1977, jzhou@mri.jhu.edu, or Jaishri Blakeley, M.D., Department of Neurology, Johns Hopkins University, 1550 Orleans Street, Suite 1M16, Baltimore, MD 21231, USA. Phone: (410) 502-3378, jblakel3@jhmi.edu.

Conflicts of Interest

J.Z. and P.C.M.v.Z. are co-inventors on a patent for the APT MRI technology. This patent is owned and managed by Johns Hopkins University. P.C.M.v.Z. is a paid lecturer for Philips Medical Systems. This arrangement has been approved by The Johns Hopkins University in accordance with its Conflict of Interest policies.

Supplementary data for this article are available at Clinical Cancer Research Online (http://clincancerres.aacrjournals.org/).

Results: Eighteen of 21 patients had recurrent tumor, and 3 had treatment effect on clinical pathology. In 12 patients, there were multiple histopathologic assignments confirmed within the same tumor. Of the 64 total specimens, 20 specimens were active glioma, 27 mixed active and quiescent glioma, and 17 quiescent/no identifiable tumor. APTw signal intensity and histopathologic assignment, cellularity, and proliferation index had significant positive correlations (R = 0.651, 0.580, and 0.458, respectively; all P < 0.001). ROC analysis with a 1.79% APTw intensity cutoff differentiated active from non-active tumor (AUC of 0.881) with 85.1% sensitivity and 94.1% specificity. Analysis of clinical pathology showed the mean APTw intensity for each patient had 94.4% sensitivity and 100% positive predictive value for identifying recurrent glioma at this cutoff.

Conclusions: APTw imaging hyperintensity may be a marker of active malignant glioma. It is able to distinguish between regions of heterogeneous abnormality on anatomical brain MRI with high sensitivity and specificity.

Keywords

recurrent glioma; treatment effect; image-guided biopsy; biomarker; APT-weighted MRI

Introduction

Malignant gliomas, such as glioblastoma (GBM) and anaplastic astrocytoma (AA), are the most common and deadly primary brain tumors in adults. Limitations in neuroimaging complicate the clinical management of patients with gliomas and impede efficient testing of new therapeutics (1, 2). Notably, existing anatomical MRI sequences are not sufficiently tissue-specific to differentiate the areas of the treatment-related changes from active cancer, both of which often show indistinguishable MRI features. Given the limitations, post-treatment patients with suspected recurrence are often referred for repeat surgery to obtain pathologic confirmation of active cancer (3). However, due to tremendous heterogeneity, choosing a representative area for tissue sampling can be very challenging, and the most active tumor tissue may be missed during a diagnostic neurosurgical procedure (4). To address these unmet clinical needs, many studies have applied advanced imaging techniques to evaluate treatment response versus active cancer, including diffusion imaging, perfusion imaging, and MR spectroscopy (5–10), as well as radiomics and machine learning (11–13). Although promising, the results, to date, have been mixed. Currently, there are no established, reliable methods with which to distinguish true tumor progression from treatment-induced changes.

Amide proton transfer-weighted (APTw) imaging, a specific type of chemical exchange saturation transfer MRI (14–16), is a molecular MRI technique that can provide contrast based on endogenous cellular proteins and peptides in tissue (17, 18). Since it was first reported in 2003, the clinical usefulness of APTw MRI has been explored for brain tumors (19–21) and other cancers (22–24). In the context of newly diagnosed gliomas, numerous early studies have shown the diagnostic values of APTw MRI in grading tumor (25–27), differentiating between tumor and peritumoral edema (28), and predicting genomic markers in gliomas, such as the isocitrate dehydrogenase mutation status and O6-methylguanine-DNA methyltransferase promoter methylation status (29, 30). Notably, a few recent

preclinical studies in rats clearly showed that untreated glioma and radiation necrosis exhibited opposite APTw signals (hyperintense vs. isointense/hypointense, respectively), and thus, could readily be distinguished by APTw signal intensity (31, 32). In addition, effects of treatment could be detected within days with APTw imaging (32, 33).

Despite the potential clinical value of APTw MRI in identifying active malignant glioma and in assessing intratumoral histopathologic heterogeneity (27), APTw-based radiographic-histopathologic validation in the post-treatment glioma setting has not been reported. This is required to advance APTw MRI as a reliable non-invasive diagnostic tool for widespread clinical use. In this study, we performed a radiopathologic correlation study via APTw image-guided stereotactic biopsy, in multiple regions of interest (ROIs) with varying APTw signal intensities in patients with suspected recurrent malignant glioma after initial treatment with chemoradiation. We hypothesized that APTw MRI would specify regions of active glioma in a heterogeneous background after chemoradiation treatment.

Materials and Methods

Human Subject Recruitment

This prospective study was approved by the Institutional Review Board and conducted in accordance with the U.S. Common Rule, and informed written consent was obtained from each subject. Between April 2010 and October 2015, 81 patients were initially recruited according to the inclusion criteria: ≥20 years old; initial diagnosis of pathologically proven primary malignant glioma; status-post initial surgery and chemoradiation (34); and suspected recurrent malignant glioma. Exclusion criteria were: non-removable metal in the body; claustrophobia; pregnant women; moderate to advanced kidney failure; and inability to give informed consent. All subjects were evaluated for study eligibility and invited to participate by two co-investigators (L.B. and J.O.B.) prior to study entry. Sixty other patients were excluded due to no repeat surgery (n = 31); surgery suspended because of the operative complication (n = 1); the interval between APTw MRI and surgery longer than one week (n = 18); no APTw MRI guidance (n = 8); and no tissue available for research (n = 2). Twenty-one patients (16 men, five women; mean age, 54.6 ± 17.0 years old; 16 GBMs, two gliosarcomas, and three AAs; see Table 1) were included in the analysis. All patients underwent the maximum feasible surgical resection, followed by radiotherapy with concomitant and adjuvant temozolomide chemotherapy (34); had a question of recurrent tumor vs. treatment effect after chemoradiation and were then referred to repeat surgery; as well as completed APTw scanning within six days prior to follow-up surgery and had full histopathologic data.

MRI Data Acquisition

Studies were performed on a 3T human MRI scanner (Achieva; Philips Medical Systems, Best, The Netherlands) using a body coil excite and a 32-channel phased-array coil for reception. An optimal volumetric APTw imaging sequence developed recently (25) was used in this study. Briefly, this sequence consists of radiofrequency saturation (four block pulses of 200 ms duration and 2 μT amplitude, the best situation that we can achieve with the current hardware (35)), lipid suppression, and three-dimensional gradient- and spin-echo

image acquisition. Other imaging parameters were: field of view (FOV), 212×186 mm^2; resolution, 2.2×2.2 mm^2; 15 slices; thickness, 4.4 mm; sensitivity-encoding acceleration factor in the right-left direction, 2; repetition time (TR), 3 sec; and specific absorption rate, 1.1 W/kg. APTw imaging was acquired with a six-offset protocol (S_0, ±3, ±3.5, ±4 ppm from water; 1, 1, 4, 1 averages, respectively) (19), which was acquired twice and averaged during data processing. More acquisitions at ±3.5 ppm were obtained to increase the APTw signal-to-noise ratio. The total scan time was 8 min 6 sec. The water saturation shift referencing method (36) was used to determine B_0 maps (range, −1.5 to 1.5 ppm; interval, 0.125 ppm; saturation power, 0.5 μT; saturation time, 200 ms; TR, 1.25 sec; scan time, 1 min 43 sec).

Several standard anatomical and advanced MR images were acquired for reference, including fluid-attenuated inversion recovery (FLAIR; TR, 11 sec; echo time or TE, 120 ms; inversion recovery time, 2.8 sec; 60 slices; thickness, 2.2 mm); T_1-weighted and gadolinium-enhanced T_1-weighted (T_1w and Gd-T_1w; three-dimensional magnetization-prepared-rapid-gradient-echo sequence; TR, 3 sec; TE, 3.7 ms; inversion recovery time, 843 ms; flip angle, 8°; 150 slices; isotropic voxel, 1.1 mm^3); as well as dynamic susceptibility-contrast (DSC) MRI (gradient-echo, echo-planar imaging sequence; TR, 1.5 sec; TE, 40 ms; 15 slices; thickness, 3.4 mm; gap, 1 mm; 40 dynamics). The injection rate for Gd contrast agents (0.2 mL/kg body weight; Magnevist; Berlex, Montville, NJ, USA) was 5 mL/sec. The Gd-T_1w imaging was the last sequence acquired.

MRI Data Processing

The APTw image analysis was performed using interactive data language (IDL, Version 7; Exelis Visual Information Solutions, Inc., Boulder, CO, USA). To reduce possible motion artifacts during the scanning, the acquired APT image series was registered to the saturated images at 3.5 ppm (37), using a rigid-body transformation with six degrees of freedom. After correcting for the B_0 inhomogeneity-based frequency shifts using the determined B_0 map from the water saturation shift-referencing method (36), the APTw image was constructed with the magnetization transfer-ratio asymmetry at the offsets of ±3.5 ppm with respect to the water signal (19): $MTR_{asym}(3.5\ ppm) = S_{sat}(-3.5\ ppm)/S_0 - S_{sat}(+3.5\ ppm)/S_0$, where S_{sat} and S_0 are the imaging signal intensities with and without selective radiofrequency irradiation, respectively. To account for the presence (mixing in) of nuclear Overhauser enhancement (NOE) effects at −3.5 ppm from various mobile and semisolid biomolecules to $MTR_{asym}(3.5ppm)$, the calculated $MTR_{asym}(3.5ppm)$ image is generally called the APTw image (19). The APTw intensity is a continuum and is reported as a percentage change in the bulk water signal intensity. DSC perfusion data were processed using FDA-approved software (Olea Sphere; Olea Medical Solutions, La Ciotat, France), and leakage-corrected cerebral blood volume (CBV) maps were obtained.

Stereotactic Biopsy

At pre-surgical planning, a neurosurgeon selected two-to-five ROIs, based on APTw and other acquired MR images. When possible, the pre-determined ROIs included both APTw hyperintense and iso-intense portions within Gd-enhancing regions. These ROIs, deemed feasible for sampling within the surgical field, were typically located in different slices.

Areas of large liquefactive necrosis, hemorrhages, or large vessels evident on standard MRI sequences were excluded. At the time of surgery, patients were placed in a Mayfield three-point head fixation device, and the BrainLab neuro-navigation system (BrainLab VectorVision2, Heimstten, Germany) was used to label and locate the biopsy targets accurately. To minimize contributions from sampling error, specimens from ROIs were always obtained prior to resection. Each specimen was 1 mm in diameter × 7.5 mm in length, a size that is routinely achieved in stereotactic biopsies. For 14 patients, the exact *de facto* sites of sampling were further confirmed by a screenshot image in real time via the BrainLab system.

Histopathologic Analysis

Hematoxylin and eosin (H&E)-stained and immunohistochemically stained biopsy specimens were reviewed, both semi-quantitatively and quantitatively, for tumor cellularity, degree of necrosis, and cell proliferation. This was performed by an experienced neuropathologist (C.G.E.) who was blinded to the imaging features. The whole H&E-stained slide was first inspected to determine the specimen-based cellularity and necrosis ($Cell_{spec}$ and Nec_{spec}). Cellularity was scored as high, moderate, low, very low, or no tumor, according to the relative density of all tumor cell nuclei. The degree of necrosis was scored as an area percentage: 0 (no necrosis); 1–25%; 26–50%; 51–75%; and 76–100%. Similar to those previously described (3, 38), multiple histopathologic features (nuclear pleomorphism, proliferation, vascular changes, and patterns of necrosis) were evaluated to assign each specimen as ($Path_{spec}$): no identifiable tumor; quiescent (inactive); “mixed” (up to 50% active tumor cells); or “active” (more than 50% active tumor cells). At the level of the patient, the integrated clinical pathologic results based on more extensive sampling of the tumor were obtained from the electronic medical record system.

For the quantitative histopathologic analysis, three hotspots were selected for each specimen, and digital images were captured by a microscope. Digital pictures for cellularity analysis were captured in a 200× magnification field on H&E-stained slides, and digital pictures for proliferation analysis were captured in a 400× magnification field on Ki-67-stained slides (MIB-1 antibody anti-Ki-67, 1:50; Dako, Hamburg, Germany). Cellularity (cells per FOV) and proliferation (% of Ki-67 positively stained nuclei) were semi-automatically counted by an “analyze particle” function in the open-source, image-processing software, ImageJ (Version 1.48; NIH, Bethesda, MD, USA). The mean values over three hotspots were recorded as quantitative parameters ($Cell_{count}$ and Ki-67). Finally, the more common terminology of recurrent tumor (i.e., active and mixed tissues) or treatment effect (i.e., quiescent and non-tumor tissues) was also used to perform a receiver operating characteristic (ROC) analysis.

Quantitative APTw Image Analysis

To obtain the APTw signal intensity for each biopsy location, the structural MR images used in the BrainLab neuro-navigation system were co-registered to the APTw images and saturated (S_{sat}) images at 3.5 ppm (37). After this, each sampling site was transferred from the clinical anatomical MR images (including the intraoperative screenshot images with the exact sampling site) to the identical site on the co-registered saturated S_{sat} image at 3.5 ppm.

The ROIs were drawn manually around the biopsy site (five-to-six voxels each) by an experienced neuroradiologist (S.J.) on these co-registered S_{sat}(3.5ppm) images. A contralateral normal-appearing white mater (CNAWM) ROI in the same slice was drawn for reference. Based on the choice of acquisition parameters, malignant glioma is associated with APTw hyperintensity (displayed as red to orange) in the APTw image, while contralateral normal-appearing white mater (CNAWM) has about zero intensity (green to blue; similar to ventricles) (39). The difference between APTw intensity values from lesion and a similar sized CNAWM region in the same slice were reported (lesion APTw - CNAWM APTw). In addition, FLAIR hyperintensity-based tumor volume (Vol_{FLAIR}), Gd-enhancing tumor volume (Vol_{Gd}), and APTw-based recurrent tumor volume (according to the cutoff APTw signal intensity in differentiating between recurrent tumor and treatment effect; Vol_{APTw}) were calculated for each patient.

Statistical Analysis

Statistical calculations were performed using SPSS software (Version 23; SPSS Inc., Chicago, IL, USA) or R software (Foundation for Statistical Computing, Vienna, Austria). The data were reported as mean ± standard deviation. Pearson's, Spearman's, or Kendall's rank correlation analysis was applied to determine the reciprocal relationships between APTw and each pathologic index, between two pathologic indices, or between APTw and relative cerebral blood volume (rCBV, defined as lesion CBV/CNAWM CBV), depending on the variable type (between continuous variables, between continuous and categorical variables, or between categorical variables, respectively). The Mann-Whitney U test was used to compare the tumor volumes for different patient groups. Generalized linear mixed model (GLMM) was used to compare APTw levels among different histopathologic categories and patient groups (fixed effects). Random intercept of patient was used where all observations from the same patient were treated as one cluster. The GLMM was fitted twice using "N" and "Q" categories as reference histopathologic categories, respectively, to get two-sided p-values. The same analysis was repeated with rCBV as the response variable. To predict cancer recurrence using APTw and/or rCBV, leave-one-out cross-validation of GLMM with logic link function was used. In this GLMM model, the fixed effects were APTw and/or rCBV while the random effect was the intercept of patient. The prediction accuracy was assessed using an area under the ROC curve (AUC). Significance levels were set at $P = 0.05$ (two-sided).

Results

Histopathologic Results

A total of 64 biopsy specimens with identifiable sampling sites were obtained from Gd contrast-enhancing regions of interest with varying APTw signal intensities in 21 patients. Ki-67 labeling was successfully performed in 60 specimens (Table 2). Based on the histopathologic analysis, 20 specimens (31%) were assigned as active tumor, 27 (42%) as a mixture of active and quiescent tumor, and 13 (20%) as quiescent tumor, and four (6%) contained no identifiable tumor. Two or more histopathologic categories (active, mixed, quiescent, or no tumor) were found within the same tumor in 12 of 21 patients (57%).

APTw Image and Histopathologic Qualitative Features

All 64 biopsied regions of interest shared similar radiographic characteristics on the routine anatomical MR images, showing heterogeneous hyperintensity on FLAIR images, polymorphic heterogeneous Gd enhancement on Gd-T_1w images, and variable degrees of mass effect. In contrast, APTw images revealed different characteristics among the ROIs with different histopathologic assignments (Fig. 1). For example, in an ROI that harbored active tumor (Fig. 1A), the APTw image was characteristically nodular and heterogeneous with substantial hyperintensity, compared to the CNAWM. Histopathologic section revealed extremely high cellularity and proliferation, with mitotic activity. In contrast, in an ROI that corresponded to quiescent tumor (Fig. 1B), the APTw image exhibited relatively homogeneous iso-intensity with a minimal amount of scattered punctate hyperintensity, compared to the CNAWM. The histopathology corresponding to these ROIs revealed extensive necrosis, and scattered quiescent tumor cells with a low level of cellularity.

Notably, heterogeneity was often observed across biopsies from different ROIs within a single patient. Figure 2 shows an example of a patient with a pathologically proven glioblastoma after craniotomy, chemoradiation, and adjuvant temozolomide. The lesion showed extensive FLAIR hyperintensity, with a centrally necrotic, peripherally enhancing component on the Gd-T_1w images, as well as heterogeneous hyperintensity on the APTw images. Three specimens were sampled from ROIs with iso-intense, intermediate, and hyperintense APTw intensities within Gd-enhancing areas. The corresponding histopathologic diagnosis was “quiescent,” “mixed,” and “active,” respectively. This patient was clinically diagnosed as having tumor recurrence, as reported in the electronic medical record system.

Correlation Analysis between APTw and Pathologic Indices

Based on the bivariate correlation analysis (Fig. 3A and B, and Supplementary Table S1), APTw intensity showed a statistically significant positive correlation with the histopathologic assignment for each specimen ($R = 0.651$; $P < 0.001$), suggesting that APTw signal intensity increased with increasing pathological evidence of active tumor (also see Supplementary Results: Regression Analysis between APTw and Pathologic Indices). In addition, APTw intensity showed significant positive correlations with $Cell_{spec}$ ($R = 0.616$; $P < 0.001$), $Cell_{count}$ ($R = 0.580$; $P < 0.001$), and the Ki-67 index ($R = 0.458$; $P < 0.001$). As the cellularity and proliferation of the specimen increased, the corresponding APTw intensities increased. In contrast, there was a weak (but significant) negative correlation between APTw intensity and treatment necrosis ($R = -0.255$; $P < 0.05$).

Accuracy of APTw MRI in Identifying Recurrent Tumor

For all 64 biopsied specimens (Fig. 3C), the mean APTw intensities of the biopsied sites that corresponded to active tissues (3.15 ± 0.55%; hyperintensity), mixed tissues (2.60 ± 0.94%), and quiescent/no tumor tissues (1.30 ± 0.54% / 1.42 ± 0.22%; iso-intensity to minimal hyperintensity) were significantly different between groups (all $P < 0.05$). Such a decreasing trend (active to quiescent or no tumor) in APTw signal intensity was similar to that observed in previous animal studies (31–33).

Based on the commonly used dichotomous histopathologic assignment (Fig. 3D), the mean APTw intensities in ROIs that represented active tumor (i.e., active and mixed tissues; 2.84 ± 0.84%) were significantly different from ROIs that represented non-active tumor (i.e., quiescent and no tumor tissues; 1.32 ± 0.48%; $P < 0.001$). The ROC curve analysis (Fig. 3E) showed that APTw MRI for the differentiation of active tumor from non-active tumor had a high AUC of 0.881 (95% confidence interval: 0.776–0.985), with an 85.1% sensitivity and a 94.1% specificity at the cutoff APTw signal intensity of 1.79%. In the same cohort of patients, the rCBV based on DSC MRI in differentiating active tumor from non-active tumor had an AUC of 0.733 (95% confidence interval: 0.591–0.876; sensitivity, 76.2%; specificity, 80.0%; cutoff, 1.56; see Supplementary Fig. S1). There was no significant correlation between these two modalities for individual specimens ($R = 0.214$, $P = 0.110$). In addition, combined the APTw and rCBV in differentiating active tumor from non-active tumor had an AUC of 0.933 (95% confidence interval: 0.869–0.998; sensitivity, 88.1%; specificity, 93.3%).

Clinical Results

The integrated clinical pathologic results from the electronic health record showed that 18/21 patients (86%) had recurrent tumor, and 3/21 (14%; patients 6, 17, and 18) had treatment effect (Table 1). Notably, analysis of the 12 specimens collected across these three treatment effect patients (Table 2) showed that 11 specimens were true negative, and one was false positive (APTw = 1.86%). APTw MRI performed better than DSC perfusion MRI (showing that nine specimens were true negative, and three were false positive). As shown in Fig. 4, the mean APTw signal intensity for the treatment effect patient group was significantly lower than that for the recurrent tumor patient group (1.24% ± 0.29% vs. 2.71% ± 0.91%; $P < 0.05$). In this small cohort of patients, the mean APTw signal intensity >1.79% for each patient corresponded to a sensitivity of 94.4%, a specificity of 100.0%, a positive predictive value of 100.0%, and a negative predictive value of 75.0% for identifying recurrent malignant glioma.

Finally, according to the cutoff APTw signal intensity (1.79%) in differentiating between active tumor and non-active tumor, it was found (Supplementary Figs. S2 and S3) that the relative APTw-based recurrent tumor volumes (with respect to the FLAIR hyperintensity-based tumor volumes) were significantly lower for the treatment effect patient group than the recurrent tumor patient group (0.07 ± 0.03 vs. 0.31 ± 0.25; $P < 0.05$).

Discussion

We investigated the radiographic-histopathologic correlation of volumetric APTw image-directed stereotactic biopsy in patients with suspected recurrent malignant glioma after initial maximal therapy. Our results indicate that APTw imaging can identify areas with the most malignant biological behavior, consistent with active tumor, within heterogeneous brain lesions. The histopathologic differentiation between recurrent tumor (active and mixed tissues) and treatment effect (quiescent and non-tumor tissues) achieved by APTw MRI was not readily feasible with several conventional anatomical MRI sequences (1), consistent with several early pre-clinical and clinical studies (31–33, 40, 41). It is particularly notable that

APTw MRI hyperintensity (defined as >1.79% in this study) had a AUC of 0.881, with an 85.1% sensitivity and a 94.1% specificity, in differentiating between recurrent glioma and treatment effect, which is similar or slightly improved diagnostic accuracy compared to other advanced MRI methods (9, 41). For example, Wang et al. (9) found that maximum rCBV had an AUC of 0.727 and a combination of diffusion tensor imaging fractional anisotropy and maximum rCBV had an AUC of 0.807 in distinguishing true progression from mixed response and pseudoprogression. Park et al. (41) reported the 90^{th} percentile normalized CBV histogram parameter for differentiating tumor progression from the treatment-related effects had AUCs of 0.80 for the expert and 0.77 for the trainee. APTw MRI is now commercially available (42). The technique, with no need for exogenous contrast, can be incorporated into standard brain tumor MRI exam protocols on 3T MRI systems, which are widely clinically available.

The APT effect is based on the concentration of endogenous mobile proteins and peptides (associated predominantly with cellularity) and exchange rate (associated with tissue pH) (17, 18). Currently, understanding the mechanism behind APTw contrast in tumor remains an interesting research topic in the field (43, 44). As discussed previously (45), the intracellular pH of active malignant glioma is near neutrality, or a little alkaline (with a slight increase of 0.05−0.08 pH unit reported). Thus, the large APT effect observed in tumor is usually dominated by the increased amide proton concentration. All patients in our study had a question of active tumor versus treatment effect after having completed standard chemoradiation (34). Although the precise mechanism of radiation and alkylating agent-induced neurotoxicity remains to be elucidated, several possibilities have been postulated, including vascular endothelial damage (46), white matter injury due to radiation damage to glial cells (38), and cytotoxicity and mutagenicity of alkylating agents through modification of the bases of DNA (47), all of which may lead to regional, perivascular, parenchymal coagulative necrosis and loss of core cellular components (48). Under these circumstances, a focal reduction in the concentration of APT-detectable mobile proteins and peptides is an ineluctable outcome (17). Based on our data, the quiescent tumor tissue, histopathologically characterized by necrosis and low proliferation, did, indeed, show significantly lower APTw intensities than the tissue representing active glioma, consistent with the preclinical results (31–33). The fact that only a moderate correlation existed between APTw and cellularity supports our notion that the APTw signal is associated with cellularity, but affected by additional factors.

Several limitations to this study should be acknowledged. First, although we obtained 64 specimens, the number of individual participants was relatively small. Second, it is widely acknowledged that brain shifts at the time of surgery may influence sampling accuracy. This cannot be fully controlled, and may have affected the spatial accuracy of the radiopathologic correlations. Our neurosurgeons took precautions to minimize the impact of brain shift from the pre-operative MRI to the time of tumor sampling, including sampling at the start of the procedure, sampling the middle of the target ROI, and taking a screenshot image when a specimen was obtained. Third, the volumetric APTw images in this study were generated at a 4.4-mm thickness with an in-plane spatial resolution of 2.2×2.2 mm^2, which presented a voxel volume size of approximately 0.02 cm^3. To increase the measurement accuracy of the APTw data with the relatively low signal-to-noise ratio and the association between the

imaging analysis and the histopathologic review, a reasonably large ROI of five-to-six voxels (namely, a rough *in vivo* tissue volume of 0.1 cm^3) was used to quantify APTw intensity values. Our data showed that there were correlations between APTw intensities and the specimen-based, or hotspot, histopathologic measurements (Fig. 3 and Supplementary Table S1). Therefore, it is anticipated that our quantitative analysis of APTw images and biopsy specimens yielded a reliable assessment that allows a meaningful interpretation of the radiographic-histopathologic correlation results. Fourth, the APTw signal quantified from the magnetization transfer-ratio asymmetry at ±3.5 ppm is always contaminated with the upfield NOE signals from mobile and semisolid proton types (including conventional semisolid magnetization transfer asymmetry) (19). Fortunately, it has been shown recently (49) that these additional asymmetry effects contribute symbiotically to the APTw contrast. Moreover, the relative APTw image signal intensity in the tumor, with respect to the CNAWM, as used in this study, is dominated by the APT effect for the pulse sequence parameters used here. Fifth, a few experimental and tissue parameters (such as saturation duration, saturation power, and T_1 of water) may affect the APTw signal. The experimental saturation settings need to be optimized and standardized across scanner manufactures. Notably, the optimal recommended RF power for APTw MRI is 2 μT (39); otherwise, the APTw contrast may not be obtained (50). Moreover, the recent results have shown that the influence of water T_1 on APT imaging of gliomas at 2 μT was actually small (45). Finally, it seems that most of APTw images have loss of signal in the frontal portions of the brain. We are not sure whether this is due to an artifact specific to the scanner type or an innate feature of APTw imaging. However, it is quite possible that APTw images are heterogeneous in the normal brain anatomy. This is another reason that we used relative APTw values in the quantitative analysis.

In conclusion, our data show that the APTw imaging hyperintensity, as a marker of active malignant glioma, has the potential to more accurately differentiate these two different outcomes after chemoradiation. In light of the tremendous biologic heterogeneity of post-treatment gliomas, the ability to identify active glioma may assist in the accurate targeting of the most malignant regions of tumor during neurosurgical procedures in the short term. As more validation studies are performed in the long term, APTw imaging may enable the non-invasive diagnosis of recurrent tumor versus treatment effect in conjunction with standard and other advanced MRI sequences.

Supplementary Material

Refer to Web version on PubMed Central for supplementary material.

Acknowledgments

The authors thank Ms. Terri Brawner, Ms. Kathleen Kahl, Ms. Ivana Kusevic, and Mr. Joe Gillen for assistance with the scanning, and Ms. Mary McAllister for editorial assistance.

Disclosure of Potential Grant Support

This work was supported in part by grants from the National Institutes of Health (R01EB009731, R01EB015032, R01CA166171, R21CA227783, R01CA228188, R01NS070024, UG3NS106937, and P41EB015909). The supporting sources had no role in the study design or conduct, or in the decision to submit for publication.

REFERENCES

1. Wen PY, Macdonald DR, Reardon DA, Cloughesy TF, Sorensen AG, Galanis E, et al. Updated response assessment criteria for high-grade gliomas: response assessment in neuro-oncology working group. J Clin Oncol. 2010;28:1963–72. [PubMed: 20231676]
2. Vogelbaum MA, Jost S, Aghi MK, Heimberger AB, Sampson JH, Wen PY, et al. Application of novel response/progression measures for surgically delivered therapies for gliomas: Response assessment in neuro-oncology (RANO) working group. Neurosurgery. 2012;70:234–43. [PubMed: 21593697]
3. Woodworth GF, Garzon-Muvdi T, Ye X, Blakeley JO, Weingart JD, Burger PC. Histopathological correlates with survival in reoperated glioblastomas. J Neuro-Oncol. 2013;113:485–93.
4. Melguizo-Gavilanes I, Bruner JM, Guha-Thakurta N, Hess KR, Puduvalli VK. Characterization of pseudoprogression in patients with glioblastoma: is histology the gold standard? J Neuro-Oncol. 2015;123:141–50.
5. Yang I, Aghi MK. New advances that enable identification of glioblastoma recurrence. Nat Rev Clin Oncol. 2009;6:648–57. [PubMed: 19806145]
6. Fatterpekar GM, Galheigo D, Narayana A, Johnson G, Knopp E. Treatment-related change versus tumor recurrence in high-grade gliomas: A diagnostic conundrum-use of dynamic susceptibility contrast-enhanced (DSC) perfusion MRI. Am J Roentgenol. 2012;198:19–26. [PubMed: 22194475]
7. Hu LS, Baxter LC, Smith KA, Feuerstein BG, Karis JP, Eschlbacher JM, et al. Relative cerebral blood volume values to differentiate high-grade glioma recurrence from posttreatment radiation effect: Direct correlation between image-guided tissue histopathology and localized dynamic susceptibility-weighted contrast-enhanced perfusion MR imaging measurements. AJNR Am J Neuroradiol. 2009;30:552–8. [PubMed: 19056837]
8. Galban CJ, Chenevert TL, Meyer CR, Tsien C, Lawrence TS, Hamstra DA, et al. Prospective analysis of parametric response map-derived MRI biomarkers: identification of early and distinct glioma response patterns not predicted by standard radiographic assessment. Clin Cancer Res. 2011;17:4751–60. [PubMed: 21527563]
9. Wang S, Martinez-Lage M, Sakai Y, Chawla S, Kim SG, Alonso-Basanta M, et al. Differentiating tumor progression from pseudoprogression in patients with glioblastomas using diffusion tensor imaging and dynamic susceptibility contrast MRI. AJNR Am J Neuroradiol. 2016;37:28–36. [PubMed: 26450533]
10. Shiroishi MS, Boxerman JL, Pope WB. Physiologic MRI for assessment of response to therapy and prognosis in glioblastoma. Neuro-Oncol. 2016;18:467–78. [PubMed: 26364321]
11. Hu XT, Wong KK, Young GS, Guo L, Wong ST. Support vector machine multiparametric MRI identification of pseudoprogression from tumor recurrence in patients with resected glioblastoma. J Magn Reson Imaging. 2011;33:296–305. [PubMed: 21274970]
12. Kickingereder P, Gotz M, Muschelli J, Wick A, Neuberger U, Shinohara RT, et al. Large-scale radiomic profiling of recurrent glioblastoma identifies an imaging predictor for stratifying anti-angiogenic treatment response. Clin Cancer Res. 2016:5765–71. [PubMed: 27803067]
13. Zhou M, Scott J, Chaudhury B, Hall L, Goldgof D, Yeom KW, et al. Radiomics in brain tumor: Image assessment, quantitative feature descriptors, and machine-learning approaches. AJNR Am J Neuroradiol. 2018;39:208–16. [PubMed: 28982791]
14. Zhou J, van Zijl PC. Chemical exchange saturation transfer imaging and spectroscopy. Progr NMR Spectr. 2006;48:109–36.
15. Kogan F, Hariharan H, Reddy R. Chemical exchange saturation transfer (CEST) imaging: Description of technique and potential clinical applications. Curr Radiol Reports. 2013;1:102–14.
16. Jones KM, Pollard AC, Pagel MD. Clinical applications of chemical exchange saturation transfer (CEST) MRI. J Magn Reson Imaging. 2018;47:11–27. [PubMed: 28792646]
17. Zhou J, Payen J, Wilson DA, Traystman RJ, van Zijl PCM. Using the amide proton signals of intracellular proteins and peptides to detect pH effects in MRI. Nature Med. 2003;9:1085–90. [PubMed: 12872167]
18. Zhou J, Lal B, Wilson DA, Laterra J, van Zijl PCM. Amide proton transfer (APT) contrast for imaging of brain tumors. Magn Reson Med. 2003;50:1120–6. [PubMed: 14648559]

19. Zhou J, Blakeley JO, Hua J, Kim M, Laterra J, Pomper MG, et al. Practical data acquisition method for human brain tumor amide proton transfer (APT) imaging. Magn Reson Med. 2008;60:842–9. [PubMed: 18816868]
20. Togao O, Yoshiura T, Keupp J, Hiwatashi A, Yamashita K, Kikuchi K, et al. Amide proton transfer imaging of adult diffuse gliomas: correlation with histopathological grades. Neuro-Oncology. 2014;16:441–8. [PubMed: 24305718]
21. Jiang S, Yu H, Wang X, Lu S, Li Y, Feng L, et al. Molecular MRI differentiation between primary central nervous system lymphomas and high-grade gliomas using endogenous protein-based amide proton transfer MR imaging at 3 Tesla. Eur Radiol. 2016;26:64–71. [PubMed: 25925361]
22. Jia G, Abaza R, Williams JD, Zynger DL, Zhou JY, Shah ZK, et al. Amide proton transfer MR imaging of prostate cancer: A preliminary study. J Magn Reson Imaging. 2011;33:647–54. [PubMed: 21563248]
23. Dula AN, Arlinghaus LR, Dortch RD, Dewey BE, Whisenant JG, Ayers GD, et al. Amide proton transfer imaging of the breast at 3 T: Establishing reproducibility and possible feasibility assessing chemotherapy response. Magn Reson Med. 2013;70:216–24. [PubMed: 22907893]
24. Takayama Y, Nishie A, Togao O, Asayama Y, Ishigami K, Ushijima Y, et al. Amide proton transfer MR imaging of endometrioid endometrial adenocarcinoma: Association with histologic grade. Radiology. 2017:DOI: 10.1148/radiol.2017170349.
25. Zhou J, Zhu H, Lim M, Blair L, Quinones-Hinojosa A, Messina AA, et al. Three-dimensional amide proton transfer MR imaging of gliomas: Initial experience and comparison with gadolinium enhancement. J Magn Reson Imaging. 2013;38:1119–28. [PubMed: 23440878]
26. Choi YS, Ahn SS, Lee SK, Chang JH, Kang SG, Kim SH, et al. Amide proton transfer imaging to discriminate between low- and high-grade gliomas: added value to apparent diffusion coefficient and relative cerebral blood volume. Eur Radiol. 2017:DOI: 10.1007/s00330-017-4732-0.
27. Jiang S, Eberhart CG, Zhang Y, Heo H-Y, Wen Z, Blair L, et al. Amide proton transfer-weighted MR image-guided stereotactic biopsy in patients with newly diagnosed gliomas. Eur J Cancer. 2017;83:9–18. [PubMed: 28704644]
28. Wen Z, Hu S, Huang F, Wang X, Guo L, Quan X, et al. MR imaging of high-grade brain tumors using endogenous protein and peptide-based contrast. NeuroImage. 2010;51:616–22. [PubMed: 20188197]
29. Jiang S, Zou T, Eberhart CG, Villalobos MAV, Heo HY, Zhang Y, et al. Predicting IDH mutation status in grade II gliomas using amide proton transfer-weighted (APTw) MRI. Magn Reson Med. 2017;78:1100–9. [PubMed: 28714279]
30. Jiang S, Rui Q, Wang Y, Heo HY, Zou T, Yu H, et al. Discriminating MGMT promoter methylation status in patients with glioblastoma employing amide proton transfer-weighted MRI metrics. Eur Radiol. 2017:DOI: 10.1007/s00330-017-5182-4.
31. Zhou J, Tryggestad E, Wen Z, Lal B, Zhou T, Grossman R, et al. Differentiation between glioma and radiation necrosis using molecular magnetic resonance imaging of endogenous proteins and peptides. Nature Med. 2011;17:130–4. [PubMed: 21170048]
32. Hong X, Liu L, Wang M, Ding K, Fan Y, Ma B, et al. Quantitative multiparametric MRI assessment of glioma response to radiotherapy in a rat model. Neuro-Oncology. 2014;16:856–67. [PubMed: 24366911]
33. Sagiyama K, Mashimo T, Togao O, Vemireddy V, Hatanpaa KJ, Maher EA, et al. In vivo chemical exchange saturation transfer imaging allows early detection of a therapeutic response in glioblastoma. Proc Natl Acad Sci (USA). 2014;111:4542–7. [PubMed: 24616497]
34. Stupp R, Mason WP, van den Bent MJ, Weller M, Fisher B, Taphoorn MJB, et al. Radiotherapy plus concomitant and adjuvant temozolomide for glioblastoma. N Engl J Med. 2005;352:987–96. [PubMed: 15758009]
35. Zhu H, Jones CK, van Zijl PCM, Barker PB, Zhou J. Fast 3D chemical exchange saturation transfer (CEST) imaging of the human brain. Magn Reson Med. 2010;64:638–44. [PubMed: 20632402]
36. Kim M, Gillen J, Landman BA, Zhou J, van Zijl PCM. Water saturation shift referencing (WASSR) for chemical exchange saturation transfer (CEST) experiments. Magn Reson Med. 2009;61:1441–50. [PubMed: 19358232]

37. Zhang Y, Heo HY, Lee DH, Zhao X, Jiang S, Zhang K, et al. Selecting the reference image for registration of CEST series. J Magn Reson Imaging. 2016;43:756–61. [PubMed: 26268435]
38. Burger PC, Dubois PJ, Schold SC, Smith KR, Odom GL, Crafts DC, et al. Computerized tomographic and pathologic studies of the untreated, quiescent, and recurrent glioblastoma-multiforme. J Neurosurg. 1983;58:159–69. [PubMed: 6294260]
39. Zhao X, Wen Z, Huang F, Lu S, Wang X, Hu S, et al. Saturation power dependence of amide proton transfer image contrasts in human brain tumors and strokes at 3 T. Magn Reson Med. 2011;66:1033–41. [PubMed: 21394783]
40. Ma B, Blakeley JO, Hong X, Zhang H, Jiang S, Blair L, et al. Applying amide proton transfer-weighted MRI to distinguish pseudoprogression from true progression in malignant gliomas. J Magn Reson Imaging. 2016;44:456–62. [PubMed: 26788865]
41. Park KJ, Kim HS, Park JE, Shim WH, Kim SJ, Smith SA. Added value of amide proton transfer imaging to conventional and perfusion MR imaging for evaluating the treatment response of newly diagnosed glioblastoma. Eur Radiol. 2016;26:4390–403. [PubMed: 26883333]
42. U.S. Food and Drug Administration, https://www.accessdata.fda.gov/cdrh_docs/pdf17/K172920.pdf.
43. Yan K, Fu Z, Yang C, Zhang K, Jiang S, Lee DH, et al. Assessing amide proton transfer (APT) MRI contrast origins in 9L gliosarcoma in the rat brain using proteomic analysis. Mol Imaging Biol. 2015;17:479–87. [PubMed: 25622812]
44. Heo HY, Lee DH, Zhang Y, Zhao X, Jiang S, Chen M, et al. Insight into the quantitative metrics of chemical exchange saturation transfer (CEST) imaging. Magn Reson Med. 2017;77:1853–65. [PubMed: 27170222]
45. Lee DH, Heo HY, Zhang K, Zhang Y, Jiang S, Zhao X, et al. Quantitative assessment of the effects of water proton concentration and water T1 changes on amide proton transfer (APT) and nuclear overhauser enhancement (NOE) MRI: The origin of the APT imaging signal in brain tumor. Magn Reson Med. 2017;77:855–63. [PubMed: 26841096]
46. Radbruch A, Weberling LD, Kieslich PJ, Eidel O, Burth S, Kickingereder P, et al. Gadolinium retention in the dentate nucleus and globus pallidus is dependent on the class of contrast agent. Radiology. 2015;275:783–91. [PubMed: 25848905]
47. Fu D, Calvo JA, Samson LD. Balancing repair and tolerance of DNA damage caused by alkylating agents. Nat Rev Cancer. 2012;12:104–20. [PubMed: 22237395]
48. Errante Y, Cirimele V, Mallio CA, Di Lazzaro V, Zobel BB, Quattrocchi CC. Progressive increase of T_1 signal intensity of the dentate nucleus on unenhanced magnetic resonance images is associated with cumulative doses of intravenously administered gadodiamide in patients with normal renal function, suggesting dechelation. Invest Radiology. 2014;49:685–90.
49. Heo HY, Zhang Y, Jiang S, Lee DH, Zhou J. Quantitative assessment of amide proton transfer (APT) and nuclear overhauser enhancement (NOE) imaging with extrapolated semisolid magnetization transfer reference (EMR) signals: II. Comparison of three EMR models and application to human brain glioma at 3 Tesla. Magn Reson Med. 2016;75:1630–9. [PubMed: 26033553]
50. Mehrabian H, Desmond KL, Soliman H, Sahgal A, Stanisz GJ. Differentiation between radiation necrosis and tumor progression using chemical exchange saturation transfer. Clin Cancer Res. 2017;23:3667–75. [PubMed: 28096269]

TRANSLATIONAL RELEVANCE

Distinguishing recurrent tumor from treatment effect following therapy for malignant gliomas remains a major clinical challenge that often leads to delays in terminating ineffective therapies or to premature termination of effective therapies. Hence, patients with suspected recurrence are frequently referred to surgery for pathologic confirmation. However, even this yields variable results depending on the region of brain sampled. Amide proton transfer-weighted (APTw) MRI is a newly emerging molecular imaging technique. Our data show that the APTw imaging hyperintensity is a surrogate marker for active malignant glioma. Use of APTw MRI, a noninvasive imaging approach that is now commercially available, may therefore assist with accurate identification of active tumor in a heterogeneous background. With future large-scale validation, this technology may obviate the need for surgery done only to confirm diagnosis or allow focal therapies to be administered only to active tumor regions.

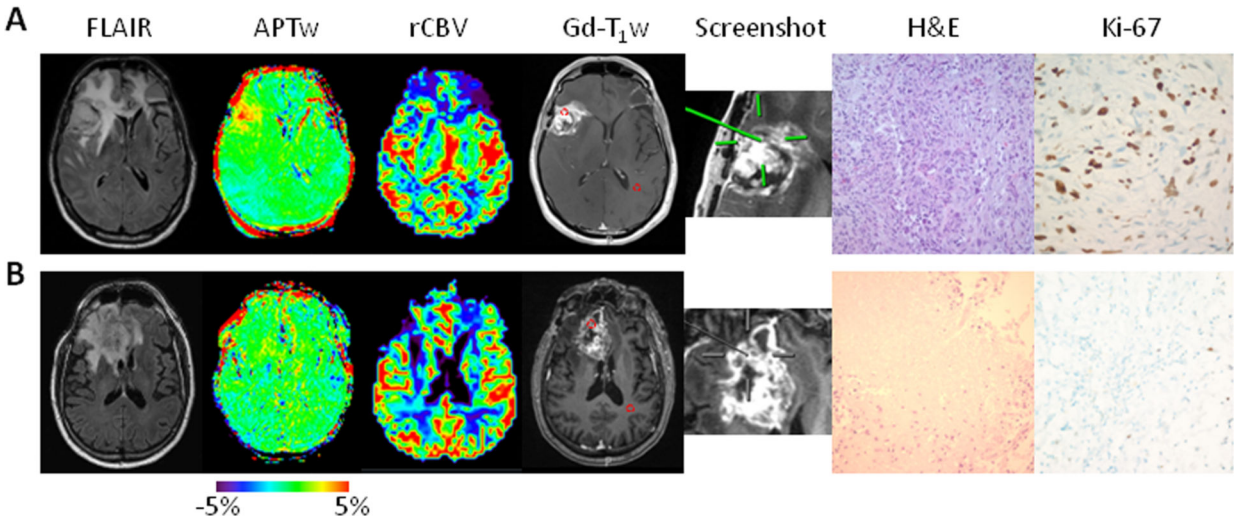

Fig. 1.

Two examples of anatomical, CBV, and APTw MR images, biopsied sites, and histology images. **A,** An active specimen obtained from a patient with a histopathologically confirmed gliosarcoma, who was treated with chemoradiation in the right frontotemporal lobe (Case 14). The biopsied site marked by a screenshot showed a heterogeneous hyperintense APTw signal (3.42%), with a high rCBV of 2.86, compared with CNAWM. The tissue obtained showed highly compacted tumor cells, and a rapid proliferation of intimately mixed neoplastic gliomatous and sarcomatous tumor cells ($Cell_{count}$ 1301 cells/FOV and proliferation 45.4%). **B,** A quiescent specimen obtained from a patient with a treated GBM in the right frontal lobe (Case 13). The biopsied site showed a homogeneous isointensity to minimal hyperintensity on the APTw image (0.87%), with an rCBV of 1.34. The specimen showed massive coagulative necrosis, reactive gliosis, inflammatory cells, and a very low cell proliferative rate ($Cell_{count}$ 230 cells/FOV and proliferation 5.7%).

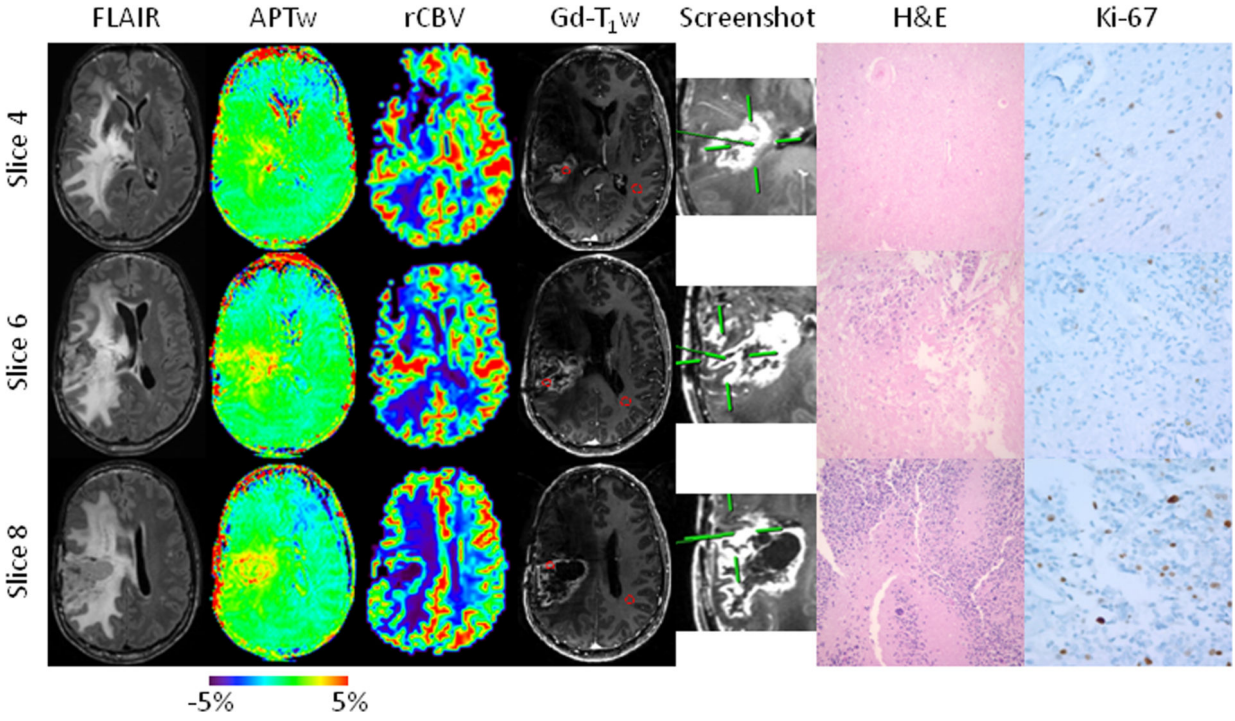

Fig. 2.

Anatomical, CBV, and APTw MR images, biopsied sites, and histology images for a patient with a treated GBM in the right parietal lobe (Case 2). Fifteen APTw slices were acquired. Three specimens were obtained from three different sites within different slices with distinct APTw signals, all with strong Gd enhancement. The specimen from Slice 4 was targeted at an APTw-isointense area (green; 1.62%), with an rCBV of 1.11, compared with CNAWM. The H&E-stained slice shows necrosis and a thickened vessel wall caused by hyalinization ($Cell_{count}$ 677 cells/FOV and proliferation 2.7%). The specimen from Slice 6 is from a mildly APTw-hyperintense spot (yellow; 1.81%), with an rCBV of 2.12. The specimen shows predominant necrosis with limited residual tumor cells ($Cell_{count}$ 876 cells/FOV and proliferation 5.1%). The specimen from Slice 8 was obtained from an APTw-hyperintense spot (yellow to red; 3.29%), with a high rCBV of 1.87. The specimen has obvious anaplasia, multinucleated tumor cells, and pseudopalisading necrosis ($Cell_{count}$ 1673 cells/FOV and proliferation 11.2%). The use of APTw image-directed biopsy can potentially reduce the randomness of surgical decisions due to tumor heterogeneity.

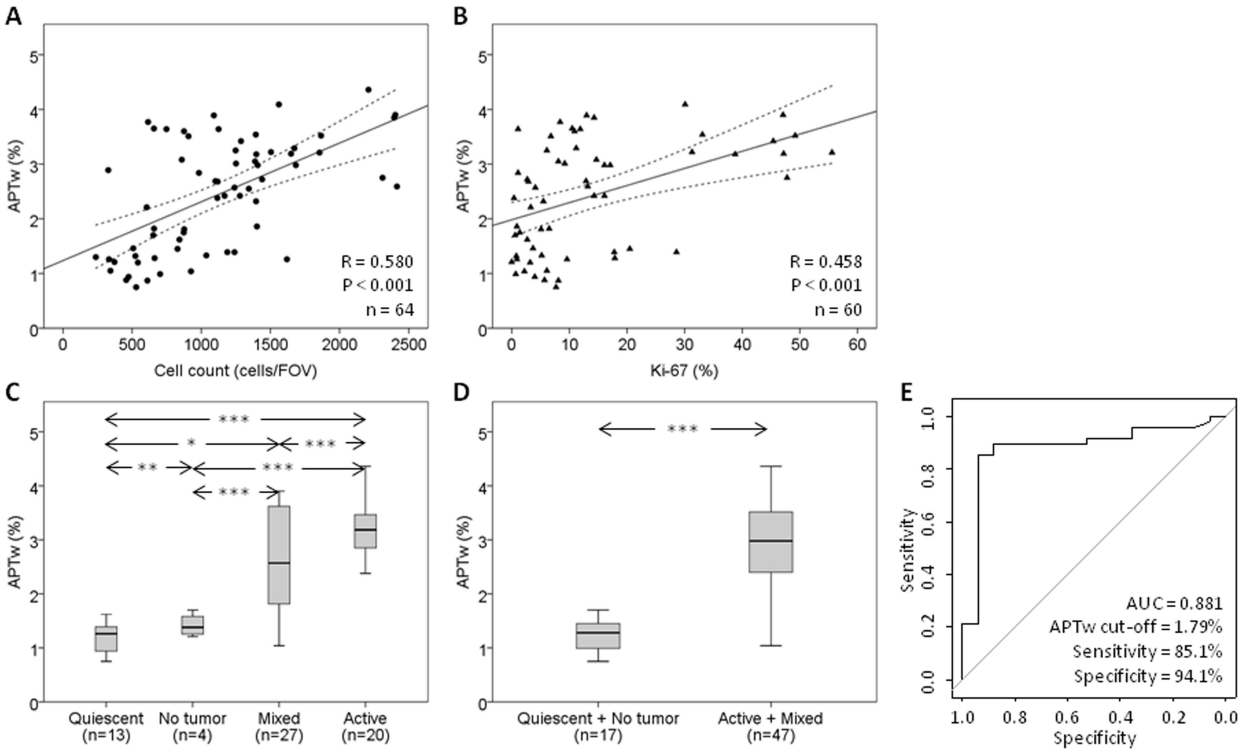

Fig. 3.

Quantitative analysis of APTw imaging intensities. **A,** Correlation of APTw intensities with $Cell_{count}$ using simple linear regression: y = 1.19 + 1.14E-3*x. **B,** Correlation of APTw intensities with Ki-67 using simple linear regression: y = 1.76 + 0.04*x. **C,** Quantitative comparison of APTw imaging intensities using box plots that correspond to quiescent, mixed, and active specimens, as well as non-tumor specimens. **D,** Quantitative comparison of APTw imaging intensities that correspond to treatment effect (non-tumor and quiescent) and tumor recurrence (mixed and active). * $P < 0.05$; ** $P < 0.01$; *** $P < 0.001$. **E,** ROC analysis of APTw imaging intensities as an imaging biomarker with which to distinguish active glioma from treatment effect.

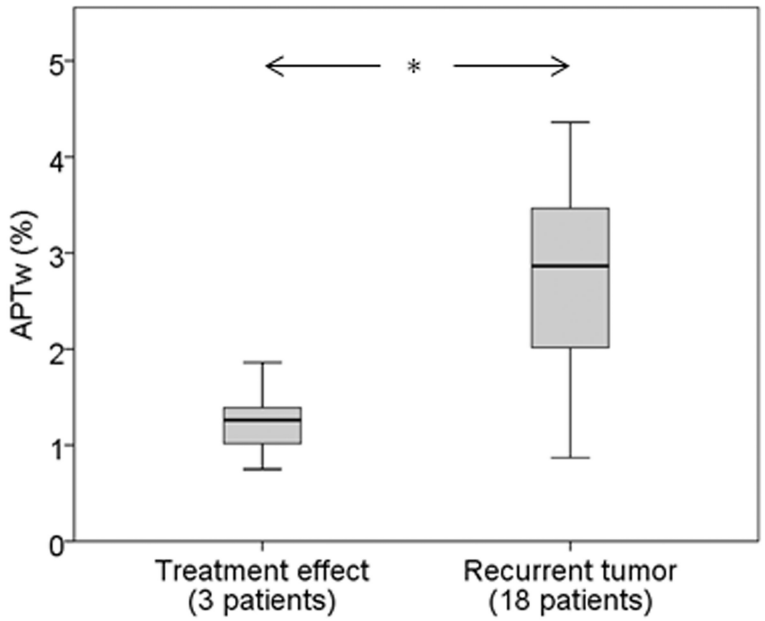

Fig. 4.

Quantitative comparison of patient-based APTw imaging intensities using box plots that correspond to three patients with treatment effect (Cases 6, 17, and 18, 12 specimens) and other 18 patients (52 specimens) with recurrent tumor. * $P < 0.05$.

Table 1.

Basic patient demographic data

Case No.	Age (yr) /Sex	Lesion Location	Initial Pathologic Diagnosis	Time Interval (day)	Operation Procedure	Integrated Clinical Diagnosis
1	38/M	Left PO	GBM	933	B&R	Recurrent tumor
2	49/M	Right P	GBM	1055	B&R	Recurrent tumor
3	42/M	Right D	GBM	225	B&R	Recurrent tumor
4	46/M	Left T	AA	142	B	Recurrent tumor
5	33/M	Left T	AA	447	B&R	Recurrent tumor
6	70/F	Right T	GBM	336	B	Treatment effect
7	52/F	Right T	GBM	353	B&R	Recurrent tumor
8	41/F	Left O	GBM	96	B&R	Recurrent tumor
9	61/M	Right P	GBM	236	B&R	Recurrent tumor
10	49/M	Left F	Gliosarcoma	89	B&R	Recurrent tumor
11	78/M	Right F	GBM	43	B&R	Recurrent tumor
12	59/M	Right OT	GBM	606	B&R	Recurrent tumor
13	68/M	Right F	GBM	181	B&R	Recurrent tumor
14	48/M	Right F	Gliosarcoma	133	B&R	Recurrent tumor
15	56/M	Right FP	GBM	797	B&R	Recurrent tumor
16	47/F	Left O	GBM	584	B&R	Recurrent tumor
17	64/M	Left FP	GBM	218	B&R	Treatment effect
18	43/M	Left O	AA	396	B&R	Treatment effect
19	49/M	Left OT	GBM	628	B&R	Recurrent tumor
20	46/M	Left F	GBM	419	B&R	Recurrent tumor
21	34/F	Left FT	GBM	1311	B&R	Recurrent tumor

Note. Tumor location: P = parietal; O = occipital; T = temporal; F = frontal; D = diencephalon. Initial pathologic diagnosis: AA = anaplastic astrocytoma; GBM = glioblastoma. Time interval: between completion of chemoradiation and APTw MRI study. Operation procedure: B = biopsy only; B&R = biopsy followed by resection. Integrated clinical diagnosis: As reported in the electronic medical record system.

Table 2.

Semi-quantitative specimen-based pathologic diagnosis results ($Path_{spec}$, $Cell_{spec}$, and Nec_{spec}), quantitative hotspot pathologic index counting results ($Cell_{count}$ and Ki-67), and the corresponding APTw and rCBV values for each specimen for all patients

Case	Specimen No.	$Path_{spec}$	$Cell_{spec}$	Nec_{spec}	$Cell_{count}$ (cells/FOV)	Ki-67 (%)	APTw (%)	rCBV
1	2	A	3	1	1649	47.2	3.19	
		Q	1	1	662	17.9	1.28	
2	3	Q	1	2	842	2.7	1.62	1.15
		M	2	3	876	5.1	1.81	1.68
		A	3	2	1673	11.2	3.29	2.87
3	2	A	4	1	1561	30.1	4.09	
		A	3	1	1398	38.8	3.18	
4	3	M	3	1	658	6.5	1.82	3.74
		M	3	1	1240	4.1	2.57	3.5
		M	3	1	1036	5.2	1.33	5.02
5	3	M	2	1	657	10.5	3.65	0.99
		M	2	1	615	8.4	3.77	1.38
		M	2	1	748	11.9	3.64	1.08
6	5	Q	1	2	541	3.2	1.20	1.36
		Q	2	1	1188	28.6	1.39	1.68
		M	3	1	1240	17.8	1.39	1.59
		Q	2	1	828	20.5	1.45	1.47
		M	1	1	332	9.6	1.26	1.45
7	5	A	4	1	2209		4.36	2.56
		M	3	2	2311	47.8	2.75	1.97
		M	3	2	2403	47.1	3.90	1.65
		M	2	1	2415	13.2	2.59	3.29
		A	3	1	1866	49.2	3.52	3.34
8	2	M	2	3	1344		2.55	2.2
		M	1	2	605	3.3	2.21	1.64
9	2	M	3	1	1125	1.1	3.64	1
		M	2	4	1091	13.0	3.89	1.16
10	4	A	3	1	1504	31.3	3.22	2.09
		M	3	1	1168	16.1	2.42	2.05
		M	3	2	2395	14.3	3.85	2.37
		M	2	1	873	1.4	1.75	1.96
11	3	A	3	1	1251	9.2	3.01	
		M	2	1	983	1.1	2.84	
		N	1	1	237		1.30	
12	3	A	3	1	1102	12.9	2.69	1.09
		A	2	1	1116	0.4	2.38	3.39

Case	Specimen No.	$Path_{spec}$	$Cell_{spec}$	Nec_{spec}	$Cell_{count}$ (cells/FOV)	Ki-67 (%)	APTw (%)	rCBV
		M	3	1	1396	5.5	2.32	2.75
13	3	M	2	1	343	6.1	1.05	1.29
		Q	2	2	610	8.1	0.87	1.21
		Q	1	3	457	5.7	0.88	1.03
14	2	A	4	1	1287	45.4	3.42	3.02
		Q	2	4	327		2.89	1.74
15	2	M	3	1	1684	16.1	2.98	2.63
		M	2	1	1279	14.3	2.42	2.02
16	2	A	3	1	1855	55.6	3.21	3.51
		A	3	1	1408	17.1	2.98	2.55
17	4	Q	1	4	702	0.7	0.99	1.13
		Q	2	2	1619	0.9	1.26	1.67
		Q	2	1	523	0.8	1.32	1.39
		Q	2	3	474	4.0	0.94	1.44
18	3	A	2	1	1402	0.9	1.86	1.16
		M	2	3	925	2.2	1.04	1.1
		Q	1	4	529	7.7	0.75	1.03
19	4	N	1	0	372	0.0	1.21	1.09
		A	3	0	1394	33.1	3.54	1.78
		M	2	0	875	10.9	3.60	1.71
		M	2	0	1248	6.1	3.25	1.64
20	3	N	1	0	508	3.7	1.46	1.25
		A	3	1	907	6.8	3.51	1.69
		N	1	0	652	0.6	1.70	1.4
21	4	A	2	0	859	14.7	3.08	1.68
		A	3	1	1440	2.7	2.72	1.52
		A	3	1	1118	2.9	2.68	1.78
		A	4	0	1389	8.1	3.05	1.72

Note: Path = histopathologic assignment (A = active; M = mixed; Q = quiescent; N = no tumor), Cell = cellularity (4 = high; 3 = moderate; 2 = low; 1 = very low; or 0 = no tumor); Nec = necrosis (0 = no necrosis; 1 = 1~25%; 2 = 26~50%; 3 = 51~75%; and 4 = 76~100%). Subscript “spec” means the specimen-based measurement from the whole slide. $Cell_{count}$ and Ki-67 were quantitatively counted by image process software semi-automatically. Notably, three ROIs from Case 13 had consistently lower APTw as well as lower rCBV, but was clinically diagnosed as tumor recurrence.